

# Probing spin hydrodynamics on a superconducting quantum simulator

Received: 24 March 2024

Accepted: 23 August 2024

Published online: 31 August 2024

 Check for updates


Yun-Hao Shi <sup>1,2,3,9</sup>, Zheng-Hang Sun<sup>1,2,9</sup>, Yong-Yi Wang <sup>1,2,9</sup>,  
Zheng-An Wang<sup>3,4</sup>, Yu-Ran Zhang<sup>5</sup>, Wei-Guo Ma <sup>1,2</sup>, Hao-Tian Liu<sup>1,2</sup>, Kui Zhao<sup>3</sup>,  
Jia-Cheng Song<sup>1,2</sup>, Gui-Han Liang<sup>1,2</sup>, Zheng-Yang Mei<sup>1,2</sup>, Jia-Chi Zhang<sup>1,2</sup>,  
Hao Li <sup>3</sup>, Chi-Tong Chen<sup>1,2</sup>, Xiaohui Song<sup>1</sup>, Jieci Wang <sup>6</sup>, Guangming Xue<sup>3</sup>,  
Haifeng Yu <sup>3</sup>, Kaixuan Huang <sup>3</sup> , Zhongcheng Xiang <sup>1,2,4</sup> ,  
Kai Xu <sup>1,2,3,4,7,8</sup> , Dongning Zheng <sup>1,2,4,7,8</sup> & Heng Fan <sup>1,2,3,4,7,8</sup> 

Characterizing the nature of hydrodynamical transport properties in quantum dynamics provides valuable insights into the fundamental understanding of exotic non-equilibrium phases of matter. Experimentally simulating infinite-temperature transport on large-scale complex quantum systems is of considerable interest. Here, using a controllable and coherent superconducting quantum simulator, we experimentally realize the analog quantum circuit, which can efficiently prepare the Haar-random states, and probe spin transport at infinite temperature. We observe diffusive spin transport during the unitary evolution of the ladder-type quantum simulator with ergodic dynamics. Moreover, we explore the transport properties of the systems subjected to strong disorder or a tilted potential, revealing signatures of anomalous subdiffusion in accompany with the breakdown of thermalization. Our work demonstrates a scalable method of probing infinite-temperature spin transport on analog quantum simulators, which paves the way to study other intriguing out-of-equilibrium phenomena from the perspective of transport.

Transport properties of quantum many-body systems driven out of equilibrium are of significant interest in several active areas of modern physics, including the ergodicity of quantum systems<sup>1–4</sup> and quantum magnetism<sup>5–7</sup>. Understanding these properties is crucial to unveil the non-equilibrium dynamics of isolated quantum systems<sup>8,9</sup>. One essential property of transport is the emergence of classical hydrodynamics in microscopic quantum dynamics, which shows the power-law tail of autocorrelation functions<sup>8</sup>. The rate of the power-law decay, referred as to the transport exponent, characterizes the universal classes of hydrodynamics. In  $d$ -dimensional quantum systems, in addition to generally expected diffusive transport with the exponent

$d/2$  in non-integrable systems<sup>10–12</sup>, more attention has been attracted by the anomalous superdiffusive<sup>5,13–16</sup> or subdiffusive transport<sup>2,3,17–19</sup>, with the exponent larger or smaller than  $d/2$ , respectively.

Over the last few decades, considerable strides have been made in enhancing the scalability, controllability, and coherence of noisy intermediate-scale quantum (NISQ) devices based on superconducting qubits<sup>20–23</sup>. With these advancements, several novel phenomena in non-equilibrium dynamics of quantum many-body systems have been observed, such as quantum thermalization<sup>24,25</sup>, ergodicity breaking<sup>26–29</sup>, time crystal<sup>30–32</sup>, and information scrambling<sup>33,34</sup>. More importantly, in this platform, the beyond-classical computation has

<sup>1</sup>Institute of Physics, Chinese Academy of Sciences, Beijing, China. <sup>2</sup>School of Physical Sciences, University of Chinese Academy of Sciences, Beijing, China. <sup>3</sup>Beijing Academy of Quantum Information Sciences, Beijing, China. <sup>4</sup>Hefei National Laboratory, Hefei, China. <sup>5</sup>School of Physics and Optoelectronics, South China University of Technology, Guangzhou, China. <sup>6</sup>Department of Physics and Key Laboratory of Low Dimensional Quantum Structures and Quantum Control of Ministry of Education, Hunan Normal University, Changsha, China. <sup>7</sup>Songshan Lake Materials Laboratory, Dongguan, China. <sup>8</sup>CAS Center for Excellence in Topological Quantum Computation, UCAS, Beijing, China. <sup>9</sup>These authors contributed equally: Yun-Hao Shi, Zheng-Hang Sun, Yong-Yi Wang.  e-mail: [huangkx@baqis.ac.cn](mailto:huangkx@baqis.ac.cn); [zcxiang@iphy.ac.cn](mailto:zcxiang@iphy.ac.cn); [kaixu@iphy.ac.cn](mailto:kaixu@iphy.ac.cn); [hfan@iphy.ac.cn](mailto:hfan@iphy.ac.cn)

been demonstrated by sampling the final Haar-random states of randomized sequences of gate operations<sup>35–39</sup>. Recently, a method of measuring autocorrelation functions at infinite temperature based on the Haar-random states has been proposed, which opens up a practical application of pseudo-random quantum circuits for simulating hydrodynamics on NISQ devices<sup>40,41</sup>.

In this work, using a ladder-type superconducting quantum simulator with up to 24 qubits, we first demonstrate that in addition to the digital pseudo-random circuits<sup>35–41</sup>, a unitary evolution governed by a time-independent Hamiltonian, i.e., an analog quantum circuit, can also generate quantum states randomly chosen from the Haar measure, i.e., the Haar-random states, for measuring the infinite-temperature autocorrelation functions<sup>42–44</sup>. Subsequently, we study the properties of spin transport on the superconducting quantum simulator via the measurement of autocorrelation functions by using the Haar-random states. Notably, we observe a clear signature of the diffusive transport on the qubit ladder, which is a non-integrable system<sup>11,12,25</sup>.

Upon subjecting the qubit ladder to disorder, a transition from delocalized phases to many-body localization (MBL) occurs as the strength of the disorder increases<sup>45</sup>. By measuring the autocorrelation functions, we experimentally probe an anomalous subdiffusive transport with intermediate values of the disorder strength. The observed signs of subdiffusion are consistent with recent numerical results and can be explained as a consequence of a Griffith-like region on the delocalized side of the MBL transition<sup>2,3,46–49</sup>.

Finally, we explore spin transport on the qubit ladder with a linear potential, and it is expected that Stark MBL occurs when the potential gradients are sufficiently large<sup>28,50–54</sup>. With a large gradient, the conservation of the dipole moment emerges<sup>28,54</sup>, associated with the phenomena known as the Hilbert space fragmentation<sup>55–57</sup>. Recent theoretical works reveal a subdiffusion in the dipole-moment conserving systems<sup>17,19</sup>. In this experiment, we present evidence of a subdiffusive regime of spin transport in the tilted qubit ladder.

## Results

### Experimental setup and protocol

Our experiments are performed on a programmable superconducting quantum simulator consisting of 30 transmon qubits with the geometry of a two-legged ladder, see Fig. 1a, b. The nearest-neighbor qubits are coupled by a fixed capacitor, and the effective Hamiltonian of capacitive interactions can be written as<sup>22,23</sup> (also see Supplementary Note 1)

$$\hat{H}_I/\hbar = \sum_{m \in \{\uparrow, \downarrow\}} \sum_{j=1}^{L-1} J_{j,m}^{\parallel} (\hat{\sigma}_{j,m}^+ \hat{\sigma}_{j+1,m}^- + \text{H.c.}) + \sum_{j=1}^L J_j^{\perp} (\hat{\sigma}_{j,\uparrow}^+ \hat{\sigma}_{j,\downarrow}^- + \text{H.c.}), \quad (1)$$

where  $\hbar = h/2\pi$ , with  $h$  being the Planck constant (in the following, we set  $\hbar = 1$ ),  $L$  is the length of the ladder,  $\hat{\sigma}_{j,m}^+$  ( $\hat{\sigma}_{j,m}^-$ ) is the raising (lowering) operator for the qubit  $Q_{j,m}$ , and  $J_{j,m}^{\parallel}$  ( $J_j^{\perp}$ ) refers to the rung (intrachain) hopping strength. For this device, the averaged rung and intrachain hopping strength are  $J^{\parallel}/2\pi \simeq 7.3$  MHz and  $J^{\perp}/2\pi \simeq 6.6$  MHz, respectively. The XY and Z control lines on the device enable us to realize the drive Hamiltonian  $\hat{H}_d = \sum_{m \in \{\uparrow, \downarrow\}} \sum_{j=1}^L \Omega_{j,m} (e^{-i\phi_{j,m}} \hat{\sigma}_{j,m}^+ + e^{i\phi_{j,m}} \hat{\sigma}_{j,m}^-)/2$ , and the on-site potential Hamiltonian  $\hat{H}_z = \sum_{m \in \{\uparrow, \downarrow\}} \sum_{j=1}^L w_{j,m} \hat{\sigma}_{j,m}^z$ , respectively. Here,  $\Omega_{j,m}$  and  $\phi_{j,m}$  denote the driving amplitude and the phase of the microwave pulse applied on the qubit  $Q_{j,m}$ , and  $w_{j,m}$  is the effective on-site potential.

To study spin transport and hydrodynamics, we focus on the equal-site autocorrelation function at infinite temperature, which is

defined as

$$C_{\mathbf{r},\mathbf{r}} = \frac{1}{D} \text{Tr} [\hat{\rho}_{\mathbf{r}}(t) \hat{\rho}_{\mathbf{r}}], \quad (2)$$

where  $\hat{\rho}_{\mathbf{r}}$  is a local observable at site  $\mathbf{r}$ ,  $\hat{\rho}_{\mathbf{r}}(t) = e^{i\hat{H}t} \hat{\rho}_{\mathbf{r}} e^{-i\hat{H}t}$ , and  $D$  is the Hilbert dimension of the Hamiltonian  $\hat{H}$ . Here, for the ladder-type superconducting simulator, we choose  $\hat{\rho}_{\mathbf{r}} = (\hat{\sigma}_{1,\uparrow}^z + \hat{\sigma}_{1,\downarrow}^z)/2$  ( $\mathbf{r}=1$ )<sup>12</sup>, and the autocorrelation function can be rewritten as

$$C_{1,1} = \frac{1}{4} (c_{1,\uparrow,1,\uparrow} + c_{1,\uparrow,1,\downarrow} + c_{1,\downarrow,1,\uparrow} + c_{1,\downarrow,1,\downarrow}), \quad (3)$$

with  $c_{\mu,\nu} = \text{Tr} [\hat{\sigma}_{\mu}^z(t) \hat{\sigma}_{\nu}^z]/D$  (subscripts  $\mu$  and  $\nu$  denote the qubit index  $1 \uparrow$  or  $1, \downarrow$ ).

The autocorrelation functions (2) at infinite temperature can be expanded as the average of  $C_{\mathbf{r},\mathbf{r}}(|\psi_0\rangle) = \langle \psi_0 | \hat{\rho}_{\mathbf{r}}(t) \hat{\rho}_{\mathbf{r}} | \psi_0 \rangle$  over different  $|\psi_0\rangle$  in  $z$ -basis. In fact, the dynamical behavior of an individual  $C_{\mathbf{r},\mathbf{r}}(|\psi_0\rangle)$  is sensitive to the choice of  $|\psi_0\rangle$  under some circumstances (see Supplementary Note 7 for the dependence of  $C_{\mathbf{r},\mathbf{r}}(|\psi_0\rangle)$  on  $|\psi_0\rangle$  in the qubit ladder with a linear potential as an example). To experimentally probe the generic properties of spin transport at infinite temperature, one can obtain (2) by measuring and averaging  $C_{\mathbf{r},\mathbf{r}}(|\psi_0\rangle)$  with different  $|\psi_0\rangle$ <sup>15</sup>. Alternatively, we employ a more efficient method to measure (2) without the need of sampling different  $|\psi_0\rangle$ . Based on the results in ref. 40 (also see “Methods”), the autocorrelation function  $c_{\mu,\nu}$  can be indirectly measured by using the quantum circuit as shown in Fig. 1c, i.e.,

$$c_{\mu,\nu} \simeq \langle \psi_{\nu}^R(t) | \hat{\sigma}_{\mu}^z | \psi_{\nu}^R(t) \rangle, \quad (4)$$

where  $|\psi_{\nu}^R(t)\rangle = \hat{U}_H(t)[|0\rangle_{\nu} \otimes |\psi^R\rangle]$  with  $|\psi^R\rangle = \hat{U}_R \otimes_{i \in Q_R} |0\rangle_i$ , and  $\hat{U}_R$  being a unitary evolution generating Haar-random states. For example, to experimentally obtain  $c_{1,\downarrow,1,\uparrow}$ , we choose  $Q_{1,\uparrow}$  as  $Q_A$ , and the remainder qubits as the  $Q_R$ . After performing the pulse sequences as shown in Fig. 1d, we measure the qubit  $Q_{1,\downarrow}$  at  $z$ -basis to obtain the expectation value of the observable  $\hat{\sigma}_{1,\downarrow}^z$ .

### Observation of diffusive transport

In this experiment, we first study spin transport on the 24-qubit ladder consisting of  $Q_{1,\uparrow}, \dots, Q_{12,\uparrow}$  and  $Q_{1,\downarrow}, \dots, Q_{12,\downarrow}$ , described by the Hamiltonian (1). For a non-integrable model, one expects that diffusive transport  $C_{1,1} \propto t^{-1/2}$  occurs<sup>12</sup>. To measure the autocorrelation function  $C_{1,1}$  defined in Eq. (3), we should first perform a quantum circuit generating the required Haar-random states  $|\psi^R\rangle$ . Instead of using the digital pseudo-random circuits in refs. 35–41, here we experimentally realize the time evolution under the Hamiltonian  $\hat{H}_R = \hat{H}_I + \hat{H}_d$ , where the parameters  $\Omega_{j,m}$  and  $\phi_{j,m}$  in  $\hat{H}_d$  have site-dependent values with the average  $\bar{\Omega}/2\pi \simeq 10.4$  MHz ( $\bar{\Omega}/J^{\parallel} \simeq 1.4$ ) and  $\bar{\phi} = 0$  (see “Methods” and Supplementary Note 3 for more details), i.e.,  $\hat{U}_R(t_R) = \exp(-i\hat{H}_R t_R)$ , which is more suitable for our analog quantum simulator. To benchmark that the final state  $|\psi^R\rangle = \hat{U}_R(t_R)|0\rangle$  can approximate the Haar-random states, we measure the participation entropy  $S_{\text{PE}} = -\sum_{k=1}^D p_k \ln p_k$ , with  $D$  being the dimension of Hilbert space,  $p_k = \langle k | \psi^R \rangle^2$ , and  $\{|k\rangle\}$  being a computational basis. Figure 2a shows the results of  $S_{\text{PE}}$  with different evolution times  $t_R$ . For the 23-qubit system, the probabilities  $p_k$  are estimated from the single-shot readout with a number of samples  $N_s = 3 \times 10^7$ . It is seen that the  $S_{\text{PE}}$  tends to the value for Haar-random states, i.e.,  $S_{\text{PE}}^T = N \ln 2 - 1 + \gamma$  with  $N=23$  being the number of qubits and  $\gamma \simeq 0.577$  as the Euler’s constant<sup>36</sup>. Moreover, for the final state  $|\psi^R\rangle$  with  $t_R = 200$  ns, the distribution of probabilities  $p_k$  satisfies the Porter-Thomas distribution (see Supplementary Note 4).

In Fig. 2b, we show the dynamics of the autocorrelation function  $C_{1,1}$  measured via the quantum circuit in Fig. 1c with  $t_R = 200$  ns. The experimental data satisfies  $C_{1,1} \propto t^{-\alpha}$ , with a transport exponent

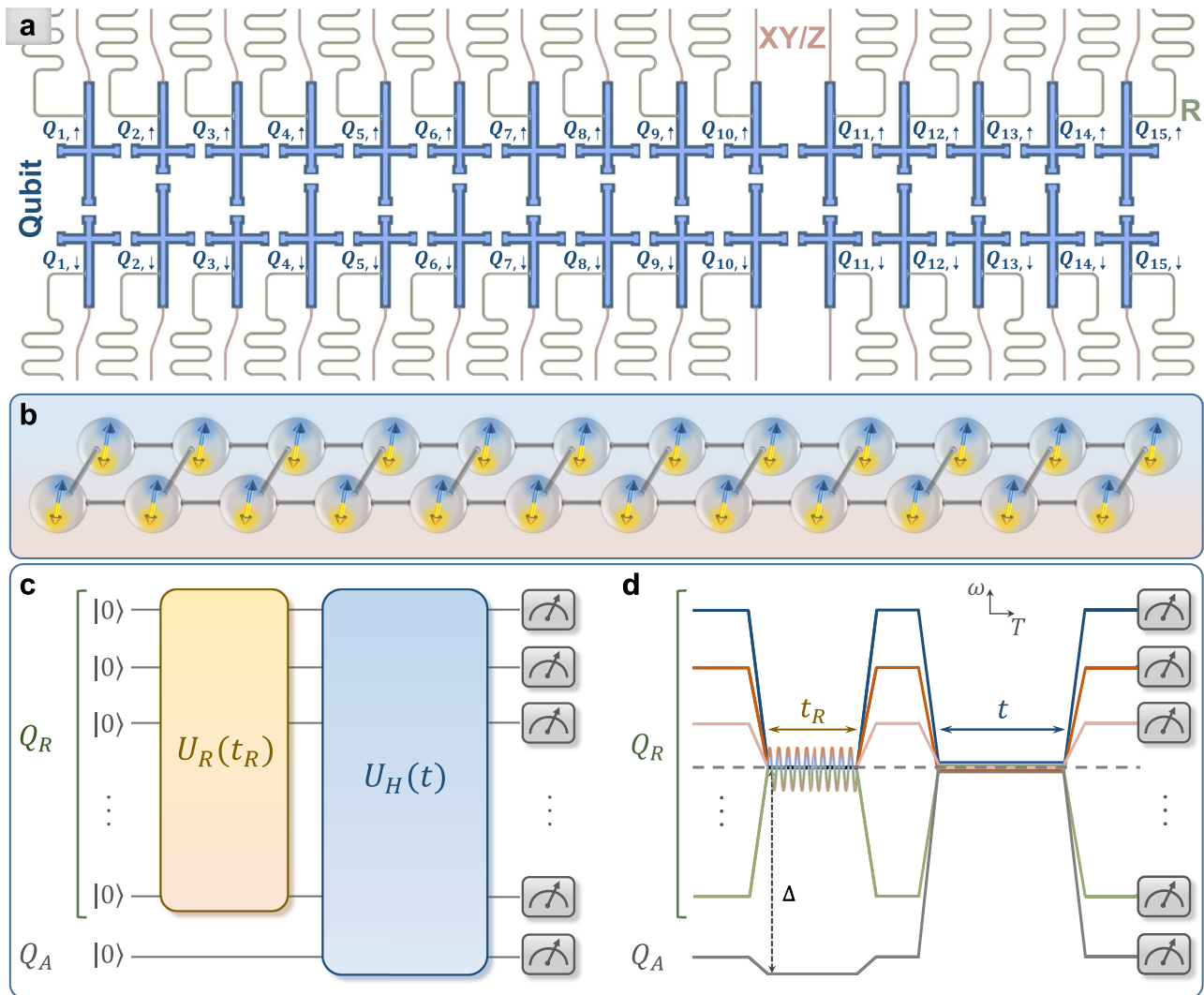


**Fig. 1 | Superconducting quantum simulator and experimental pulse sequences.** **a** The schematic showing the ladder-type superconducting quantum simulator, consisting of 30 qubits (the blue region), labeled  $Q_{1,\uparrow}$  to  $Q_{15,\uparrow}$  and  $Q_{1,\downarrow}$  to  $Q_{15,\downarrow}$ . Each qubit is coupled to a separate readout resonator (the green region), and has an individual control line (the red region) for both the XY and Z controls. **b** Schematic diagram of the simulated 24 spins coupled in a ladder. The blue and yellow double arrows represent the infinite-temperature spin hydrodynamics without preference for spin orientations. **c** Schematic diagram of the quantum circuit for measuring the autocorrelation functions at infinite temperature. All qubits are initialized at the state  $|0\rangle$ . Subsequently, an analog quantum circuit  $\hat{U}_R(t_R)$  acts on the set of qubits  $Q_R$  to generate Haar-random states. This is followed

by a time evolution of all qubits, i.e.,  $\hat{U}_H(t) = \exp(-i\hat{H}t)$  with  $\hat{H}$  being the Hamiltonian of the system, in which the properties of spin transport are of our interest. **d** Experimental pulse sequences corresponding to the quantum circuit in (c) displayed in the frequency ( $\omega$ ) versus time ( $T$ ) domain. To realize  $\hat{U}_R(t_R)$ , qubits in the set  $Q_R$  are tuned to the working point (dashed horizontal line) via Z pulses, and simultaneously, the resonant microwave pulses represented as the sinusoidal line are applied to  $Q_R$  through the XY control lines. Meanwhile, the qubit  $Q_A$  is detuned from the working point with a large value of the frequency gap  $\Delta$ . To realize the subsequent evolution  $\hat{U}_H(t)$  with the Hamiltonian (1), all qubits are tuned to the working point.

$\alpha \approx 0.5067$ , estimated by fitting the data in the time window  $t \in [50$  ns, 200 ns]. Our experiments clearly show that spin diffusively transports on the qubit ladder  $\hat{H}_I(1)$ , and demonstrate that the analog quantum circuit  $\hat{U}_R(t_R)$  with  $t_R = 200$  ns can provide sufficient randomness to measure the autocorrelation function defined in Eq. (2) and probe infinite-temperature spin transport. We also discuss the influence of  $t_R$  in Supplementary Note 4, numerically showing that the results of  $C_{1,1}$  do not substantially change for longer  $t_R > 200$  ns. Moreover, in Supplementary Note 4, we show that for a shortly evolved time  $t_R \approx 15$  ns, the values of the observable defined in Eq. (4) are incompatible with the infinite-temperature autocorrelation functions. Given that the chosen initial state for generating the Haar-random state exhibits a high effective temperature associated with the Hamiltonian  $\hat{H}_R$ , the state would asymptotically converge to the Haar-random state with a sufficiently extended  $t_R$ . However, with  $t_R \approx 15$  ns,

the time scale is too small to get rid of the coherence, and the value of  $S_{PE}$  for the state  $|\psi^R\rangle$  is much smaller than the  $S_{PE}^T$  (see Fig. 2a), suggesting that  $|\psi^R\rangle$  with  $t_R \approx 15$  ns is far away from the Haar-random state, and cannot be employed to measure the infinite-temperature autocorrelation function (2). In the following, we fix  $t_R = 200$  ns, and study spin transport in other systems with ergodicity breaking.

### Subdiffusive transport with ergodicity breaking

After demonstrating that the quantum circuit shown in Fig. 1c can be employed to measure the infinite-temperature autocorrelation function  $C_{1,1}$ , we study spin transport on the superconducting qubit ladder with the disorder, whose effective Hamiltonian can be written as  $\hat{H}_D = \hat{H}_I + \sum_{m \in \{\uparrow, \downarrow\}} \sum_{j=1}^L w_{j,m} \hat{\sigma}_{j,m}^+ \hat{\sigma}_{j,m}^-$ , with  $w_{j,m}$  drawn from a uniform distribution  $[-W, W]$ , and  $W$  is the strength of disorder. For each disorder strength, we consider 10 disorder realizations and plot the

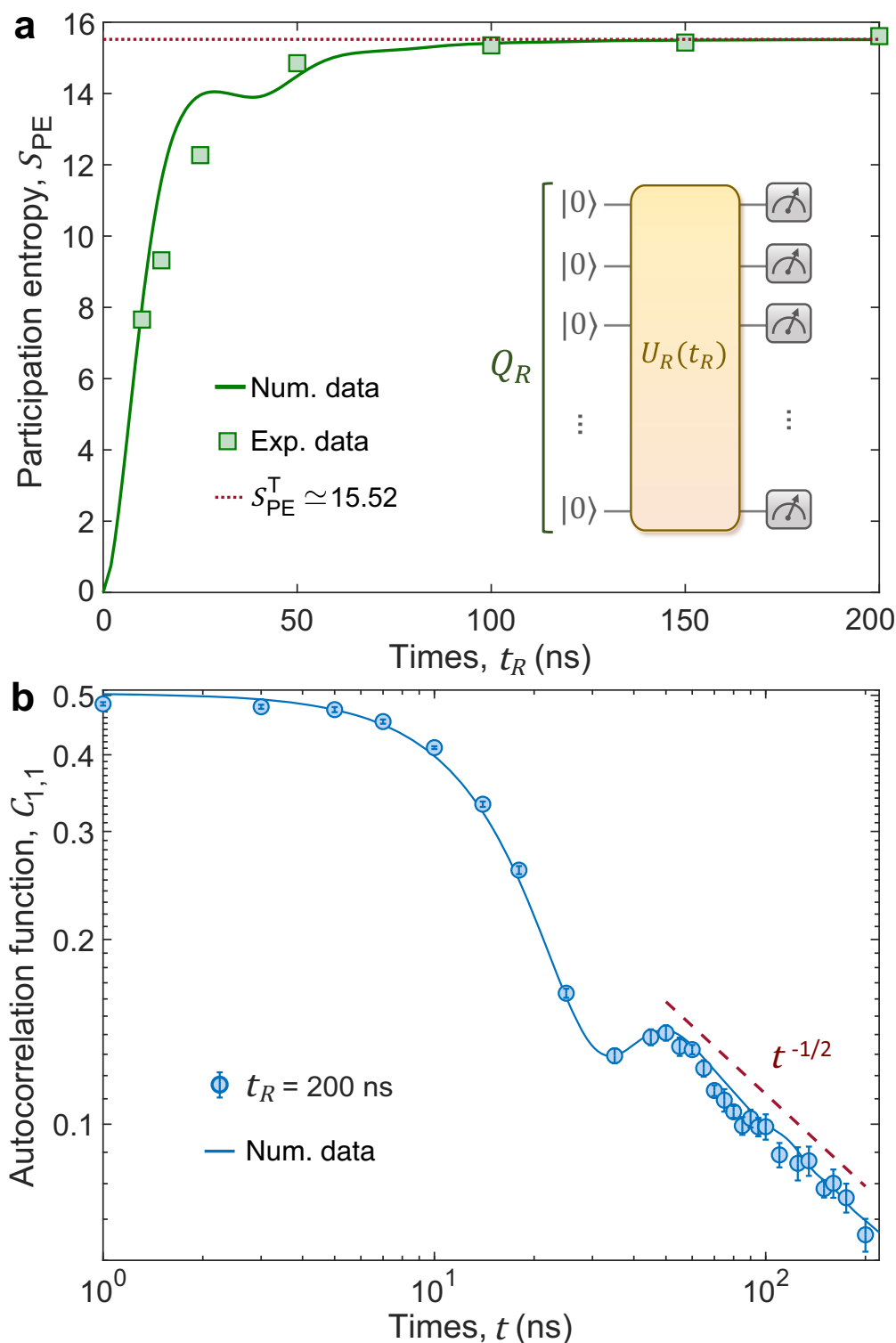


**Fig. 2 | Observation of diffusive transport.** **a** Experimental verification of preparing the states via the time evolution of participation entropy. Here, we chose  $Q_R = \{Q_{1,\uparrow}, Q_{2,\uparrow}, \dots, Q_{12,\uparrow}, Q_{2,\downarrow}, Q_{3,\downarrow}, \dots, Q_{12,\downarrow}\}$  with total 23 qubits. The inset of **(a)** shows the corresponding quantum circuit. The dotted horizontal line represents the participation entropy for Haar-random states, i.e.,  $S_{PE}^T \simeq 15.519$ . **b** Experimental results of the autocorrelation function  $C_{1,1}(t)$  for the qubit ladder with  $L = 12$ , which

are measured by performing the quantum circuit shown in Fig. 1c, d. Here, we consider the state generated from  $\hat{U}_R(t_R)$  with  $t_R = 200$  ns, which is approximate to a Haar-random state. Markers are experimental data. The solid line is the numerical simulation of the correlation function  $C_{1,1}$  at infinite temperature. The dashed line represents a power-law decay  $t^{-1/2}$ . Error bars represent the standard deviation.

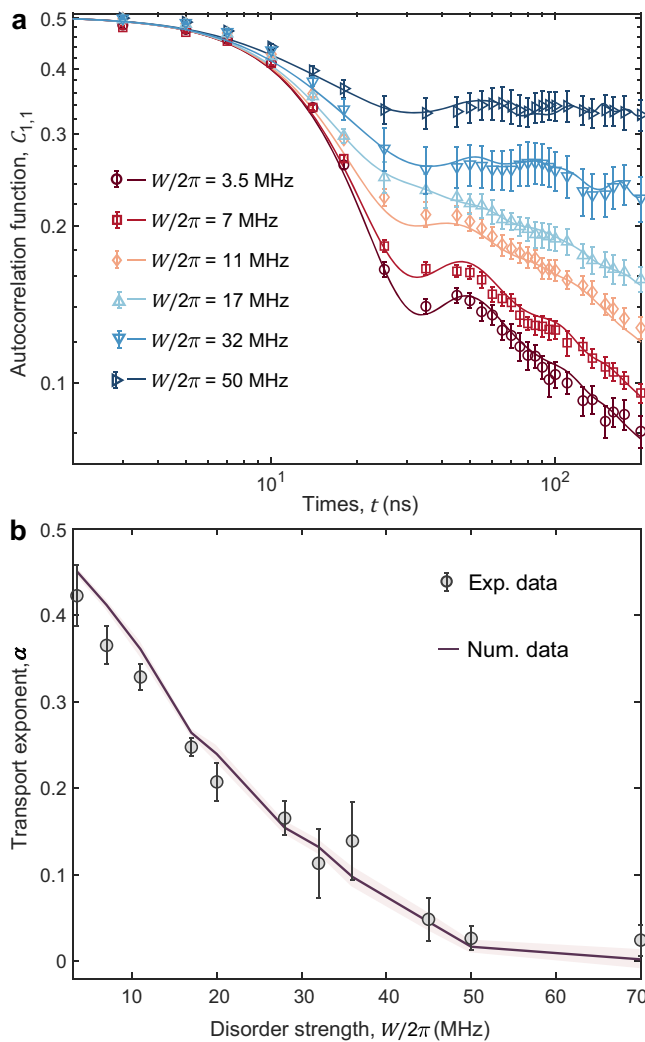


**Fig. 3 | Subdiffusive transport on the superconducting qubit ladder with disorder.** **a** The time evolution of autocorrelation function  $C_{1,1}(t)$  for the qubit ladder with  $L = 12$  and different values of disorder strength  $W$ , ranging from  $W/2\pi = 3.5$  MHz ( $W/J \approx 0.5$ ) to  $W/2\pi = 70$  MHz ( $W/J \approx 9.6$ ). Markers (lines) are experimental (numerical) data. **b** Transport exponent  $\alpha$  as a function of  $W$  obtained from fitting the data of  $C_{1,1}(t)$ . Error bars (experimental data) and shaded regions (numerical data) represent the standard deviation.

dynamics of averaged  $C_{1,1}$  with different  $W$  are plotted in Fig. 3a. With the increasing of  $W$ , and as the system approaches the MBL transition,  $C_{1,1}$  decays more slowly. Moreover, the oscillation in the dynamics of  $C_{1,1}$  becomes more obvious with larger  $W$ , which is related to the presence of local integrals of motion in the deep many-body localized phase<sup>58</sup>.

We then fit both the experimental and numerical data with the time window  $t \in [50 \text{ ns}, 200 \text{ ns}]$  by adopting the power-law decay  $C_{1,1} \propto t^{-\alpha}$ . As shown in Fig. 3b, we observe an anomalous subdiffusive region with the transport exponent  $\alpha < 1/2$ . For the strength of disorder  $W/2\pi \geq 50$  MHz, the transport exponent  $\alpha \sim 10^{-2}$  indicates the freezing of spin transport and the onset of MBL on the 24-qubit system<sup>2</sup>. Here, we emphasize that the estimated transition point between the subdiffusive regime and MBL is a lower bound since, with longer evolved time, the exponent  $\alpha$  obtained from the power-law fitting becomes slightly larger (see Supplementary Note 6).

Next, we explore the transport properties on a tilted superconducting qubit ladder, which is subjected to the linear potential  $\hat{H}_L = \sum_{j=1}^L \Delta_j \sum_{m \in \{\uparrow, \downarrow\}} \hat{\sigma}_{j,m}^+ \hat{\sigma}_{j,m}^-$ , with  $\Delta = 2W_S/(L-1)$  being the slope of

the linear potential (see the tilted ladder in the inset of Fig. 4a). Thus, the effective Hamiltonian of the tilted superconducting qubit ladder can be written as  $\hat{H}_T = \hat{H}_I + \hat{H}_L$ . Different from the aforementioned breakdown of ergodicity induced by the disorder, the non-ergodic behaviors induced by the linear potential arise from strong Hilbert-space fragmentation<sup>55–57</sup>. The ergodicity breaking in the disorder-free system  $\hat{H}_T$  is known as the Stark MBL<sup>28,50–54</sup>.

We employ the method based on the quantum circuit shown in Fig. 1c to measure the time evolution of the autocorrelation function  $C_{1,1}$  with different slopes of the linear potential. The results are presented in Fig. 4a, b. Similar to the system with the disorder, the dynamics of  $C_{1,1}$  still satisfies  $C_{1,1} \propto t^{-\alpha}$  with  $\alpha < 0.5$ , i.e., subdiffusive transport. Figure 4c displays the transport exponent  $\alpha$  with different strengths of the linear potential, showing that  $\alpha$  asymptotically drops as  $W_S$  increases.

Two remarks are in order. First, by employing the same standard for the onset of MBL induced by disorder, i.e.,  $\alpha \sim 10^{-2}$ , the results in Fig. 4c indicate that the Stark MBL on the tilted 24-qubit ladder occurs when  $W_S/2\pi \geq 80$  MHz ( $\Delta/2\pi \geq 14.6$  MHz). Second, on the ergodic side ( $W_S/2\pi < 80$  MHz and  $W/2\pi < 50$  MHz for the tilted and disordered systems, respectively), the transport exponent  $\alpha$  exhibits rapid decay with increasing  $W_S$  up to  $W_S/2\pi \approx 20$  MHz in the tilted system. Subsequently, as  $W_S$  continues to increase, the decay of  $\alpha$  becomes slower. In contrast, for the disordered system,  $\alpha$  consistently decreases with increasing disordered strength  $W$ . We note that the impact of the emergence of dipole-moment conservation with increasing the slope of linear potential on the spin transport, and its distinction from the transport in disordered systems remains unclear and deserve further theoretical studies.

## Discussion

Based on the novel protocol for simulating the infinite-temperature spin transport using the Haar-random state<sup>40</sup>, we have experimentally probed diffusive transport on a 24-qubit ladder-type programmable superconducting processor. Moreover, when the qubit ladder is subject to sufficiently strong disorder, we observe the signatures of subdiffusive transport, accompanied by the breakdown of ergodicity due to MBL.

It is worthwhile to emphasize that previous experimental studies of the Stark MBL mainly focus on the dynamics of imbalance<sup>50,59,60</sup>. Different from the disorder-induced MBL with a power-law decay of imbalance observed in the subdiffusive Griffith-like region<sup>61</sup>, for the Stark MBL, there is no experimental evidence for the power-law decay of imbalance<sup>50,59,60</sup>. Here, by measuring the infinite-temperature autocorrelation function, we provide solid experimental evidence for the subdiffusion in tilted systems, which is induced by the emergence of strong Hilbert-space fragmentation<sup>55–57</sup>. Theoretically, it has been suggested that for a thermodynamically large system, non-zero tilted potentials, i.e.,  $\Delta > 0$ , will lead to a subdiffusive transport with  $\alpha \approx 1/4$ <sup>17,62</sup>. In finite-size systems, both results, as shown in Fig. 4 and the cold atom experiments on the tilted Fermi-Hubbard model<sup>63</sup> demonstrate a crossover from the diffusive regime to the subdiffusive one. Investigating how this crossover scales with increasing system size is a further experimental task, which requires quantum simulators with a larger number of qubits.

Ensembles of Haar-random pure quantum states have several promising applications, including benchmarking quantum devices<sup>42,64</sup> and demonstrating beyond-classical computation<sup>35–39</sup>. Our work displays a practical application of the randomly distributed quantum state, i.e., probing the infinite-temperature spin transport. In contrast to employing digital random circuits, where the number of imperfect two-qubit gates is proportional to the qubit number<sup>36–41</sup>, the scalable analog circuit adopted in our experiments can also generate multi-qubit Haar-random states useful for simulating hydrodynamics. The protocol employed in our work can be naturally extended to explore the non-trivial transport properties on other analog quantum simulators, including the Rydberg atoms<sup>42,65–67</sup>, quantum gas microscopes<sup>68,69</sup>, and the superconducting circuits with a central resonance bus, which enables long-range interactions<sup>21,70,71</sup>.

## Methods

### Derivation of Eq. 4

Here, we present the details of the derivation of Eq. (4), which is based on the typicality<sup>12,40,72</sup>. According to Eq. (2),  $c_{\mu,\nu} = \text{Tr}[\hat{\sigma}_\mu^z(t)\hat{\sigma}_\nu^z]/D$ , with  $D = 2^N$ . We define  $\hat{N}_\nu = (\hat{\sigma}_\nu^z + 1)/2$ , and then  $c_{\mu,\nu} = \frac{1}{D} \text{Tr}[\hat{\sigma}_\mu^z(t)\hat{N}_\nu]$ . By using  $\hat{N}_\nu = (\hat{N}_\nu)^2$ , we have  $c_{\mu,\nu} = \frac{1}{D} \text{Tr}[\hat{N}_\nu\hat{\sigma}_\mu^z(t)\hat{N}_\nu]$ . We note that  $\hat{N}_\nu$  is an operator which projects the state of the  $\nu$ -th qubit to the state  $|0\rangle$ .

According to the typicality<sup>12,40,72</sup>, the trace of an operator  $\hat{O}$  can be approximated as the expectation value averaged by the pure Haar-random state  $|r\rangle$ , i.e.,

$$\frac{1}{D} \text{Tr}[\hat{O}] = \langle r|\hat{O}|r\rangle + \mathcal{O}(2^{-N/2}), \quad (5)$$

with  $N$  being the number of qubits. It indicates that the infinite-temperature expectation value  $\text{Tr}[\hat{O}]/D$  can be better estimated by the expectation value for the Haar-random state  $\langle r|\hat{O}|r\rangle$ . Thus,  $c_{\mu,\nu} \simeq \langle r|\hat{N}_\nu\hat{\sigma}_\mu^z(t)\hat{N}_\nu|r\rangle = \langle \psi_\mu^R(t)|\hat{\sigma}_\mu^z|\psi_\nu^R(t)\rangle$  for multi-qubit systems. Based on the definition of the projector  $\hat{N}_\nu$ ,  $|r\rangle$  is a Haar-random state for the whole system except for the  $\nu$ -th qubit, and in the experiment, only a  $(N - 1)$ -qubit Haar-random state is required.

### Numerical simulations

Here, we present the details of the numerical simulations. We calculate the unitary time evolution  $|\psi(t + \Delta t)\rangle = e^{-iH\Delta t}|\psi(t)\rangle$  by employing the Krylov method<sup>49</sup>. The Krylov subspace is spanned by the vectors

defined as  $\{|\psi(t)\rangle, \hat{H}|\psi(t)\rangle, \hat{H}^2|\psi(t)\rangle, \dots, \hat{H}^{(m-1)}|\psi(t)\rangle\}$ . Then, the Hamiltonian  $\hat{H}$  in the Krylov subspace becomes a  $m$ -dimensional matrix  $H_m = K_m^\dagger H K_m$ , where  $H$  denotes the Hamiltonian  $\hat{H}$  in the matrix form, and  $K_m$  is the matrix whose columns contain the orthonormal basis vectors of the Krylov space. Finally, the unitary time evolution can be approximately simulated in the Krylov subspace as  $|\psi(t + \Delta t)\rangle \simeq K_m^\dagger e^{-iH_m\Delta t} K_m |\psi(t)\rangle$ . In our numerical simulations, the dimension of the Krylov subspace  $m$  is adaptively adjusted from  $m = 6$  to 30, making sure the numerical errors are smaller than  $10^{-14}$ .

For the numerical simulation of the  $\hat{U}_R(t_R) = e^{-i\hat{H}_d t_R}$  in Fig. 1c, based on the experimental data of the XY drive, the parameters in  $\hat{H}_d$  are  $\Omega_{j,m}/2\pi = 10.4 \pm 1.6$  MHz, and  $\phi_{j,m} \in [-\pi/10, \pi/10]$ .

### Details of generating Haar-random states

In this section, we present more details about the generation of faithful Haar-random states. The analog quantum circuit employed to generate Haar-random states is  $\hat{U}_R = \exp[-i(\hat{H}_J + \hat{H}_d)t]$ , where  $\hat{H}_J$  is given by Eq. (1) and  $\hat{H}_d = \sum_{m \in \{\uparrow, \downarrow\}} \sum_{j=1}^L \Omega_{j,m} (e^{-i\phi_{j,m}} \hat{\sigma}_{j,m}^+ + e^{i\phi_{j,m}} \hat{\sigma}_{j,m}^-)/2$  is the drive Hamiltonian.

Here, we first numerically study the influence of the driving amplitude  $\Omega_{j,m}$ . For convenience, we consider  $\phi_{j,m} = 0$ , and isotropic driving amplitude, i.e.,  $\Omega = \Omega_{j,m}$  for all  $(j, m)$ . We chose  $Q_R = \{Q_{1,\uparrow}, Q_{2,\uparrow}, \dots, Q_{12,\uparrow}, Q_{2,\downarrow}, Q_{3,\downarrow}, \dots, Q_{12,\downarrow}\}$  with total 23 qubits. The dynamics of participation entropy  $S_{PE}$  for different values of  $\Omega$  are plotted in Fig. 5a, and the values of  $S_{PE}$  with the evolved time  $t = 200$  ns and 1000 ns are displayed in Fig. 5b. It is seen that for small  $\Omega$ , the

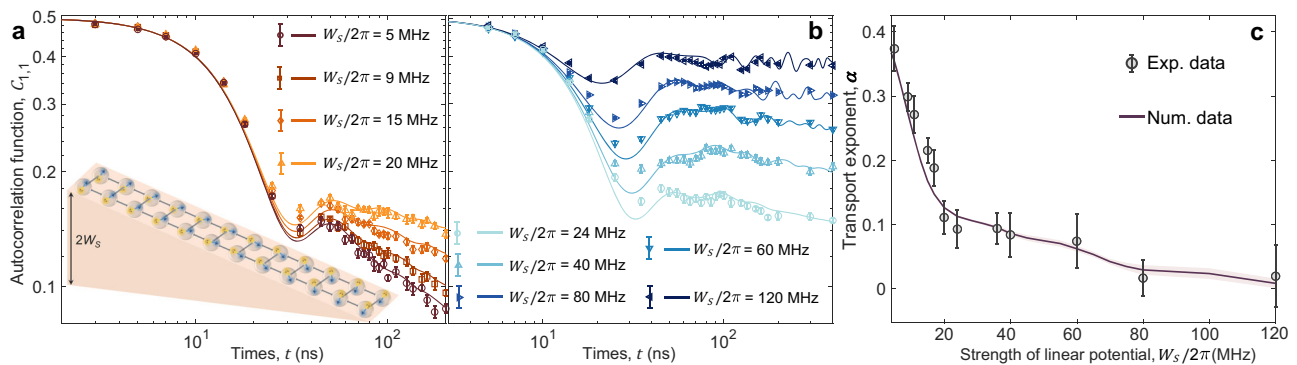


**Fig. 4 | Subdiffusive transport on the superconducting qubit ladder with linear potential.** **a** Time evolution of autocorrelation function  $C_{1,1}(t)$  for the tilted qubit ladder with  $L = 12$  and  $W_s/2\pi \leq 20$  MHz. **b** is similar to **(a)** but for the data with  $W_s/2\pi \geq 24$  MHz. Markers (lines) are experimental (numerical) data. **c** Transport

exponent  $\alpha$  as a function of  $W_s$ . For  $W_s/2\pi \leq 20$  MHz and  $W_s/2\pi \geq 24$  MHz, the exponent  $\alpha$  is extracted from fitting the data of  $C_{1,1}(t)$  with the time window  $t \in [50 \text{ ns}, 200 \text{ ns}]$  and  $t \in [100 \text{ ns}, 400 \text{ ns}]$ , respectively. Error bars (experimental data) and shaded regions (numerical data) represent the standard deviation.

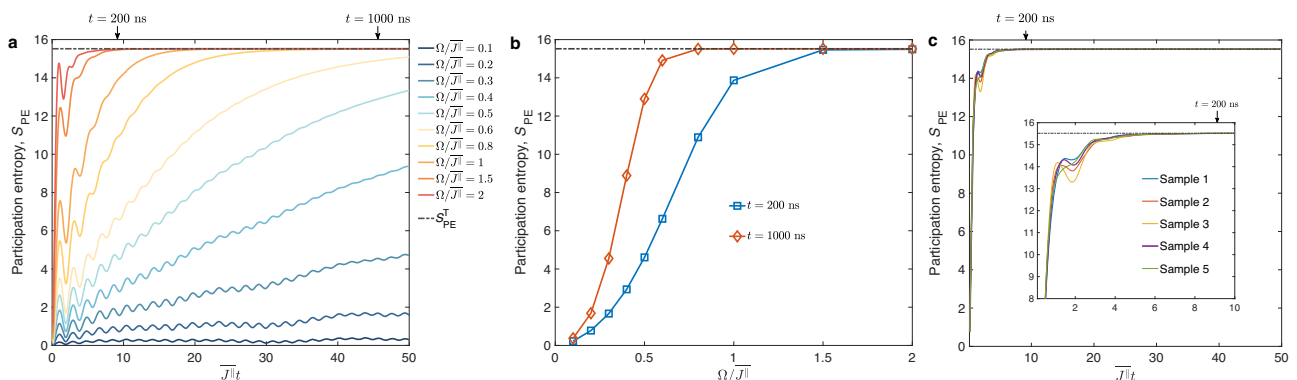


**Fig. 5 | Impact of driving amplitude and phases of microwave pulse on the generation of Haar-random states.** **a** The time evolution of the participation entropy  $S_{PE}$  for different driving amplitude  $\Omega$ . **b** The value of  $S_{PE}$  at two evolved times  $t = 200$  ns and 1000 ns, as a function of  $\Omega$ . **c** The dynamics of  $S_{PE}$  with the

phases of the microwave pulse drawn from  $[-\pi, \pi]$ . Here, we present the numerical data of 5 different samples of the phases. The inset shows the dynamics in a shorter time interval. The horizontal dashed line represents the participation entropy for Haar-random states  $S_{PE}^T \simeq 15.519$ .

growth of  $S_{\text{PE}}$  is slow and with increasing  $\Omega$ , it becomes more rapid. In this experiment, we chose  $\overline{\Omega}/J^{\parallel} \simeq 1.4$  because the participation entropy can achieve  $S_{\text{PE}}^{\text{T}}$  with a relatively short evolved time  $t \simeq 200$  ns. As  $\Omega$  further increases, the time when  $S_{\text{PE}}^{\text{T}}$  is reached does not significantly become shorter. Based on the above discussions,  $\overline{\Omega}/J^{\parallel} \simeq 1.4$  is an appropriate choice of the driving amplitude.

Next, we numerically study the influence of the randomness for the phases of driving microwave pulse  $\phi_{j,m}$ . In this experiment, by using the correction of crosstalk, the randomness of the phases is small, i.e.,  $\phi_{j,m} \in [-\pi/10, \pi/10]$ . Here, we consider the phases with large randomness, i.e.,  $\phi_{j,m} \in [-\pi, \pi]$ . The numerical results for the time evolution of  $S_{\text{PE}}$  with 5 samples of  $\phi_{j,m}$  are plotted in Fig. 5c. With  $\phi_{j,m} \in [-\pi, \pi]$ , the participation entropy can still tend to  $S_{\text{PE}}^{\text{T}}$  around 200 ns. Only the short-time behaviors are slightly different from each other for the 5 samples (see the inset of Fig. 5c).

## Data availability

The authors declare that the data supporting the findings of this study are available within the paper and its Supplementary Information files. Should any raw data files be needed in another format, they are available from the corresponding author upon reasonable request. Source data are provided in this paper.

## References

- Nandkishore, R. & Huse, D. A. Many-body localization and thermalization in quantum statistical mechanics. *Annu. Rev. Condens. Matter Phys.* **6**, 15–38 (2015).
- Agarwal, K., Gopalakrishnan, S., Knap, M., Müller, M. & Demler, E. Anomalous diffusion and Griffiths effects near the many-body localization transition. *Phys. Rev. Lett.* **114**, 160401 (2015).
- Žnidarič, M., Scardicchio, A. & Varma, V. K. Diffusive and subdiffusive spin transport in the ergodic phase of a many-body localizable system. *Phys. Rev. Lett.* **117**, 040601 (2016).
- Ljubotina, M., Desaulles, J.-Y., Serbyn, M. & Papić, Z. Superdiffusive energy transport in kinetically constrained models. *Phys. Rev. X* **13**, 011033 (2023).
- Scheie, A. et al. Detection of Kardar–Parisi–Zhang hydrodynamics in a quantum Heisenberg spin-1/2 chain. *Nat. Phys.* **17**, 726–730 (2021).
- Žnidarič, M. Spin transport in a one-dimensional anisotropic Heisenberg model. *Phys. Rev. Lett.* **106**, 220601 (2011).
- Dupont, M., Sherman, N. E. & Moore, J. E. Spatiotemporal crossover between low- and high-temperature dynamical regimes in the quantum Heisenberg magnet. *Phys. Rev. Lett.* **127**, 107201 (2021).
- Bertini, B. et al. Finite-temperature transport in one-dimensional quantum lattice models. *Rev. Mod. Phys.* **93**, 025003 (2021).
- Eisert, J., Friesdorf, M. & Gogolin, C. Quantum many-body systems out of equilibrium. *Nat. Phys.* **11**, 124–130 (2015).
- Peng, P., Ye, B., Yao, N. Y., and Cappellaro, P. Exploiting disorder to probe spin and energy hydrodynamics. *Nat. Phys.* <https://doi.org/10.1038/s41567-023-02024-4> (2023).
- Steinigeweg, R., Heidrich-Meisner, F., Gemmer, J., Michielsen, K. & De Raedt, H. Scaling of diffusion constants in the spin- $\frac{1}{2}$  XX ladder. *Phys. Rev. B* **90**, 094417 (2014).
- Schubert, D. et al. Quantum versus classical dynamics in spin models: Chains, ladders, and square lattices. *Phys. Rev. B* **104**, 054415 (2021).
- Ljubotina, M., Žnidarič, M. & Prosen, Tomaž. Spin diffusion from an inhomogeneous quench in an integrable system. *Nat. Commun.* **8**, 16117 (2017).
- Wei, D. et al. Quantum gas microscopy of Kardar–Parisi–Zhang superdiffusion. *Science* **376**, 716–720 (2022).
- Joshi, M. K. et al. Observing emergent hydrodynamics in a long-range quantum magnet. *Science* **376**, 720–724 (2022).
- Rosenberg, E. et al. Dynamics of magnetization at infinite temperature in a Heisenberg spin chain. *Science* **384**, 48–53 (2024).
- Feldmeier, J., Sala, P., De Tomasi, G., Pollmann, F. & Knap, M. Anomalous diffusion in dipole- and higher-moment-conserving systems. *Phys. Rev. Lett.* **125**, 245303 (2020).
- De Nardis, J., Gopalakrishnan, S., Vasseur, R. & Ware, B. Subdiffusive hydrodynamics of nearly integrable anisotropic spin chains. *Proc. Natl. Acad. Sci. USA* **119**, e2202823119 (2022).
- Gromov, A., Lucas, A. & Nandkishore, R. M. Fracton hydrodynamics. *Phys. Rev. Res.* **2**, 033124 (2020).
- Ma, R. et al. A dissipatively stabilized Mott insulator of photons. *Nature* **566**, 51–57 (2019).
- Zhang, X., Kim, E., Mark, D. K., Choi, S. & Painter, O. A superconducting quantum simulator based on a photonic-bandgap metamaterial. *Science* **379**, 278–283 (2023).
- Xiang, Zhong-Cheng et al. Simulating Chern insulators on a superconducting quantum processor. *Nat. Commun.* **14**, 5433 (2023).
- Gu, X., Kockum, Anton Frisk, Miranowicz, A., Liu, Yu-xi & Nori, F. Microwave photonics with superconducting quantum circuits. *Phys. Rep.* **718–719**, 1–102 (2017).
- Chen, F. et al. Observation of strong and weak thermalization in a superconducting quantum processor. *Phys. Rev. Lett.* **127**, 020602 (2021).
- Zhu, Q. et al. Observation of thermalization and information scrambling in a superconducting quantum processor. *Phys. Rev. Lett.* **128**, 160502 (2022).
- Roushan, P. et al. Spectroscopic signatures of localization with interacting photons in superconducting qubits. *Science* **358**, 1175–1179 (2017).
- Guo, Q. et al. Observation of energy-resolved many-body localization. *Nat. Phys.* **17**, 234–239 (2021).
- Guo, Q. et al. Stark many-body localization on a superconducting quantum processor. *Phys. Rev. Lett.* **127**, 240502 (2021).
- Zhang, P. et al. Many-body Hilbert space scarring on a superconducting processor. *Nat. Physics* **19**, 120–125 (2023).
- Zhang, X. et al. Digital quantum simulation of Floquet symmetry-protected topological phases. *Nature* **607**, 468–473 (2022).
- Mi, X. et al. Time-crystalline eigenstate order on a quantum processor. *Nature* **601**, 531–536 (2022).
- Frey, P. & Rachel, S. Realization of a discrete time crystal on 57 qubits of a quantum computer. *Sci. Adv.* **8**, eabm7652 (2022).
- Mi, X. et al. Information scrambling in quantum circuits. *Science* **374**, 1479–1483 (2021).
- Braumüller, J. et al. Probing quantum information propagation with out-of-time-ordered correlators. *Nat. Phys.* **18**, 172–178 (2022).
- Neill, C. et al. A blueprint for demonstrating quantum supremacy with superconducting qubits. *Science* **360**, 195–199 (2018).
- Boixo, S. et al. Characterizing quantum supremacy in near-term devices. *Nat. Phys.* **14**, 595–600 (2018).
- Arute, F. et al. Quantum supremacy using a programmable superconducting processor. *Nature* **574**, 505–510 (2019).
- Wu, Y. et al. Strong quantum computational advantage using a superconducting quantum processor. *Phys. Rev. Lett.* **127**, 180501 (2021).
- A., Morvan et al. Phase transition in random circuit sampling. Preprint at <https://doi.org/10.48550/arXiv.2304.11119> (2023).
- Richter, J. & Pal, A. Simulating hydrodynamics on noisy intermediate-scale quantum devices with random circuits. *Phys. Rev. Lett.* **126**, 230501 (2021).
- Keenan, N., Robertson, N. F., Murphy, T., Zhuk, S. & Gool, J. Evidence of Kardar–Parisi–Zhang scaling on a digital quantum simulator. *Npj Quantum Inf.* **9**, 72 (2023).

42. Choi, J. et al. Preparing random states and benchmarking with many-body quantum chaos. *Nature* **613**, 468–473 (2023).
43. Karamlou, A. H. et al. Probing entanglement in a 2D hard-core Bose-Hubbard lattice. *Nature* **629**, 561–566 (2024).
44. Yanay, Y., Braumüller, J., Gustavsson, S., Oliver, W. D. & Tahan, C. Two-dimensional hard-core Bose-Hubbard model with superconducting qubits. *Npj Quantum Inf.* **6**, 58 (2020).
45. Sun, Z.-H., Cui, J. & Fan, H. Characterizing the many-body localization transition by the dynamics of diagonal entropy. *Phys. Rev. Res.* **2**, 013163 (2020).
46. Khait, I., Gazit, S., Yao, N. Y. & Auerbach, A. Spin transport of weakly disordered heisenberg chain at infinite temperature. *Phys. Rev. B* **93**, 224205 (2016).
47. Gopalakrishnan, S., Agarwal, K., Demler, E. A., Huse, D. A. & Knap, M. Griffiths effects and slow dynamics in nearly many-body localized systems. *Phys. Rev. B* **93**, 134206 (2016).
48. Setiawan, F., Deng, D.-L. & Pixley, J. H. Transport properties across the many-body localization transition in quasiperiodic and random systems. *Phys. Rev. B* **96**, 104205 (2017).
49. Luitz, D. J. & Lev, Y. B. The ergodic side of the many-body localization transition. *Ann. Phys.* **529**, 1600350 (2017).
50. Morong, W. et al. Observation of Stark many-body localization without disorder. *Nature* **599**, 393–398 (2021).
51. Schulz, M., Hooley, C. A., Moessner, R. & Pollmann, F. Stark Many-Body Localization. *Phys. Rev. Lett.* **122**, 040606 (2019).
52. van Nieuwenburg, E., Baum, Y. & Refael, G. From Bloch oscillations to many-body localization in clean interacting systems. *Proc. Natl. Acad. Sci.* **116**, 9269–9274 (2019).
53. Wang, Y.-Y., Sun, Z.-H. & Fan, H. Stark many-body localization transitions in superconducting circuits. *Phys. Rev. B* **104**, 205122 (2021).
54. Taylor, S. R., Schulz, M., Pollmann, F. & Moessner, R. Experimental probes of Stark many-body localization. *Phys. Rev. B* **102**, 054206 (2020).
55. Doggen, E. V. H., Gornyi, I. V. & Polyakov, D. G. Stark many-body localization: Evidence for Hilbert-space shattering. *Phys. Rev. B* **103**, L100202 (2021).
56. Khemani, V., Hermele, M. & Nandkishore, R. Localization from Hilbert space shattering: From theory to physical realizations. *Phys. Rev. B* **101**, 174204 (2020).
57. Sala, P., Rakovszky, T., Verresen, R., Knap, M. & Pollmann, F. Ergodicity breaking arising from Hilbert space fragmentation in dipole-conserving Hamiltonians. *Phys. Rev. X* **10**, 011047 (2020).
58. Serbyn, M., Papić, Z. & Abanin, D. A. Local conservation laws and the structure of the many-body localized states. *Phys. Rev. Lett.* **111**, 127201 (2013).
59. Scherg, S. et al. Observing non-ergodicity due to kinetic constraints in tilted Fermi-Hubbard chains. *Nat. Commun.* **12**, 4490 (2021).
60. Kohlert, T. et al. Exploring the regime of fragmentation in strongly tilted Fermi-Hubbard chains. *Phys. Rev. Lett.* **130**, 010201 (2023).
61. Bordia, P. et al. Probing slow relaxation and many-body localization in two-dimensional quasiperiodic systems. *Phys. Rev. X* **7**, 041047 (2017).
62. Nandy, S. et al. Emergent dipole moment conservation and subdiffusion in tilted chains. *Phys. Rev. B* **109**, 115120 (2024).
63. Guardado-Sanchez, E. et al. Subdiffusion and heat transport in a tilted two-dimensional Fermi-Hubbard system. *Phys. Rev. X* **10**, 011042 (2020).
64. Cross, A. W., Bishop, L. S., Sheldon, S., Nation, P. D. & Gambetta, J. M. Validating quantum computers using randomized model circuits. *Phys. Rev. A* **100**, 032328 (2019).
65. Saffman, M., Walker, T. G. & Mølmer, K. Quantum information with Rydberg atoms. *Rev. Mod. Phys.* **82**, 2313–2363 (2010).
66. Browaeys, A. & Lahaye, T. Many-body physics with individually controlled Rydberg atoms. *Nat. Phys.* **16**, 132–142 (2020).
67. Henriot, L. et al. Quantum computing with neutral atoms. *Quantum* **4**, 327 (2020).
68. Kaufman, A. M. et al. Quantum thermalization through entanglement in an isolated many-body system. *Science* **353**, 794–800 (2016).
69. Gross, C. & Bloch, I. Quantum simulations with ultracold atoms in optical lattices. *Science* **357**, 995–1001 (2017).
70. Xu, K. et al. Probing dynamical phase transitions with a superconducting quantum simulator. *Sci. Adv.* **6**, <https://doi.org/10.1126/sciadv.aba4935> (2020).
71. Xu, K. et al. Metrological characterization of non-gaussian entangled states of superconducting qubits. *Phys. Rev. Lett.* **128**, 150501 (2022).
72. Jin, F. et al. Random state technology. *J. Phys. Soc. Jpn.* **90**, 012001 (2020).

## Acknowledgements

We thank Hai-Long Shi and H. S. Yan for their helpful discussions. Z.X., D.Z., K.X., and H.F. are supported by the Beijing Natural Science Foundation (Grant No. Z200009), National Natural Science Foundation of China (Grants Nos. 92265207, T2121001, 12122504, 12247168, 11934018, T2322030), Innovation Program for Quantum Science and Technology (Grant No. 2021ZD0301800), Beijing Nova Program (Nos. 20220484121, 2022000216). Y.-H.S. acknowledges the support of the Postdoctoral Fellowship Program of CPSF (Grant No. GZB20240815). Z.-A.W. acknowledges the support of the China Postdoctoral Science Foundation (Grant No. 2022TQ0036).

## Author contributions

H.F. supervised the project. Z.-H.S. proposed the idea. Y.-H.S. conducted the experiment with the help of K.H. and K.X. Z.-H.S., Y.-Y.W., and Y.-H.S. performed the numerical simulations. Z.X. and D.Z. fabricated the ladder-type sample. X.S., G.X., and H.Y. provided the Josephson parametric amplifiers. W.-G.M., H.-T.L., K.Z., J.-C.S., G.-H.L., Z.-Y.M., J.-C.Z., H.L., and C.-T.C. helped the experimental setup. Z.-A.W., Y.-R.Z., J.W., K.X., and H.F. discussed and commented on the manuscript. Z.-H.S., Y.-H.S., Y.-Y.W., Y.-R.Z., and H.F. co-wrote the manuscript. All authors contributed to the discussions of the results and development of the manuscript.

## Competing interests

The authors declare no competing interests.

## Additional information

**Supplementary information** The online version contains supplementary material available at <https://doi.org/10.1038/s41467-024-52082-2>.

**Correspondence** and requests for materials should be addressed to Kaixuan Huang, Zhongcheng Xiang, Kai Xu or Heng Fan.

**Peer review information** *Nature Communications* thanks Amir Karamlou, and the other anonymous reviewer(s) for their contribution to the peer review of this work. A peer review file is available.

**Reprints and permissions information** is available at <http://www.nature.com/reprints>

**Publisher's note** Springer Nature remains neutral with regard to jurisdictional claims in published maps and institutional affiliations.



**Open Access** This article is licensed under a Creative Commons Attribution-NonCommercial-NoDerivatives 4.0 International License, which permits any non-commercial use, sharing, distribution and reproduction in any medium or format, as long as you give appropriate credit to the original author(s) and the source, provide a link to the Creative Commons licence, and indicate if you modified the licensed material. You do not have permission under this licence to share adapted material derived from this article or parts of it. The images or other third party material in this article are included in the article's Creative Commons licence, unless indicated otherwise in a credit line to the material. If material is not included in the article's Creative Commons licence and your intended use is not permitted by statutory regulation or exceeds the permitted use, you will need to obtain permission directly from the copyright holder. To view a copy of this licence, visit <http://creativecommons.org/licenses/by-nc-nd/4.0/>.

© The Author(s) 2024